research papers

Effect of convergent beam semiangle on image intensity in HAADF STEM images

Koji Kuramochi,[a] Yasutoshi Kotaka,[b] Takashi Yamazaki,[b]* Masahiro Ohtsuka,[a] Iwao Hashimoto[a] and Kazuto Watanabe[c]

[a]Department of Physics, Tokyo University of Science, Tokyo 162-8601, Japan, [b]Device and Materials Laboratories, Fujitsu Laboratories Ltd, Atsugi 243-0197, Japan, and [c]Tokyo Metropolitan College of Industrial Technology, Tokyo 140-0011, Japan. Correspondence e-mail: yamazakit@jp.fujitsu.com

In this study, we experimentally and theoretically show that the intensities of bright spots in a spherical aberration (C_s)-uncorrected high-angle annular dark-field (HAADF) scanning transmission electron microscope (STEM) image of [011]-oriented Co_3O_4, which has two different numbers of Co atoms in the projected atomic columns, are reversed with increasing sample thickness. However, C_s-corrected HAADF STEM images produce intensities that correctly depend on the average number of atoms in the projected atomic columns. From an analysis based on the Bloch-wave theorem, it is found that an insufficient semiangle of the incident convergent beam yields intensities that do not depend on the average atomic number in the atomic columns.

1. Introduction

In the last few decades, many researchers (Howie, 1979; Kirkland *et al.*, 1987; Pennycook & Boatner, 1988; Pennycook & Jesson, 1990; McGibbon *et al.*, 1994; Pennycook & Nellist, 1999; Anderson *et al.*, 1997; Yamazaki *et al.*, 2000; Ishizuka, 2001; Voyles *et al.*, 2002; Peng *et al.*, 2004; LeBeau *et al.*, 2008) have achieved spatial resolutions as high as 0.2 nm in high-angle annular dark-field (HAADF) scanning transmission electron microscopy (STEM); these resolutions are comparable to those of conventional high-resolution transmission electron microscopy. High-resolution HAADF STEM images have two main advantages: they do not exhibit contrast reversal against the defocus value and sample thickness, and the intensity of the bright spot depends on the atomic number of the atoms in the atomic column. It is also known that artificial bright spots do not appear in such images as long as the defocus is maintained in a suitable range (Watanabe, Yamazaki, Kikuchi *et al.*, 2001). In addition, such images are not affected by the Fresnel interference effect (Nakanishi *et al.*, 2004) and they do not exhibit high sensitivity to the tilting of a crystal (Yamazaki *et al.*, 2002). An HAADF STEM image is almost described by the incoherent thermal diffuse scattering (TDS). Therefore, the image obtained can be considered to be a map of the high-angle scattering power of a specimen (Pennycook & Nellist, 1999). Consequently, an HAADF STEM image enables us to identify the individual atomic columns in a crystal as well as defect structures such as dislocation cores or surfaces (Mitsuishi *et al.*, 1999; Kawasaki *et al.*, 2001; Ohtomo *et al.*, 2002; Yu *et al.*, 2004; Yamazaki *et al.*, 2004; Kuramochi, Suzuki *et al.*, 2008).

Recently, sub-ångström resolution microscopy has been attempted using a spherical aberration (C_s) corrector (Haider *et al.*, 1998; Batson *et al.*, 2002; Hutchison *et al.*, 2002; Sawada *et al.*, 2005; Dellby *et al.*, 2001). In addition to having a high spatial resolution, such images simplify the direct interpretation of the atomic arrangement because the signal-to-noise ratio is sufficiently high. Therefore, structural analyses for determining the type and number of atoms in a projected atomic column can be performed intuitively using the bright-spot contrast (Falke *et al.*, 2004; Sato *et al.*, 2006; Li *et al.*, 2007; Shibata *et al.*, 2007; Tanaka *et al.*, 2008; Smith, 2008), although dynamical simulations including both high-angle elastic scattering and TDS make the technique more quantitative. We have already investigated the effect of the chromatic aberration (C_c) coefficient on a C_s-corrected HAADF STEM image and developed a simple method for measuring this coefficient (Kuramochi *et al.*, 2009); therefore, semi-quantitative structural analyses can be performed on the nanometre scale from a comparison between the experimental C_s-corrected HAADF STEM images and their corresponding simulated images that include the effects of the C_c coefficient and spatial incoherence.

The effect of the sample thickness is one of the important factors that need to be considered for the quantitative analysis, because the intensity ratio in a sample comprising more than two elements varies with the sample thickness (LeBeau *et al.*, 2008). Thus far, the intensity of the bright spot in an atomic resolution HAADF STEM image has been considered to be highly sensitive to the average atomic number in the projected atomic columns. Recently, it was suggested that the contrast of a C_s-uncorrected HAADF STEM image cannot be intuitively

interpreted based on the atomic number (Voyles *et al.*, 2004; LeBeau *et al.*, 2009). In this study, we experimentally and theoretically show that the intensities of bright spots in C_s-uncorrected HAADF STEM images of [011]-oriented Co_3O_4, which has two different numbers of Co atoms occupying the projected atomic columns, are reversed with increasing sample thickness. Improving the optimum semiangle using the C_s corrector leads to bright-spot intensities that depend on the average number of atoms in the projected atomic columns.

2. Experimental procedures and simulation

In this study, we used reagent-grade CoO powder mixed by ball milling. The mixed powder was pressed into a pellet and sintered at 1173 K for 2 h to form a compact ceramic body. For the TEM observations, a thin specimen was cut into a disc having a diameter of 3 mm, following which it was mechanically ground and polished to a thickness of ~100 µm; a dimple ~20 µm thick was then formed at the center of the disc. The TEM sample was produced by ion milling with 5.0 keV Ar^+ ions at an incidence angle of $8°$ until a tiny perforation was formed on the central area of the disc; this was followed by bombardment with 2.0 keV Ar^+ ions at the lowest possible incident angle to produce large electron-transport regions and remove amorphous and damaged regions from the specimen.

A conventional HAADF STEM observation was carried out by using a JEM-2100F TEM/STEM (Jeol, Japan) at an operating voltage of 200 keV; the probe-forming lens had a C_s coefficient of 1.1 mm (Yamazaki, Kotaka *et al.*, 2006). The angular range of the annular detector was 36–96 mrad and the semiangle of the incident convergent beam was 11.2 mrad, which was measured using the microdiffraction method (Yamazaki *et al.*, 2002). The C_s-corrected HAADF STEM observation was carried out using the same microscope in combination with a C_s corrector (CEOS, Germany). The C_s coefficient was −0.5 µm, the angular range of the annular detector was 70–185 mrad and the semiangle of the incident convergent beam was 20.0 mrad. In the present experiment, we used two different experimental conditions to obtain the C_s-uncorrected and C_s-corrected HAADF STEM images. An angle close to the optimum semiangle of the incident convergent beam was used for observation of C_s-uncorrected HAADF STEM images. For C_s-corrected HAADF STEM images, the condition under which the highest-quality image was obtained was used, as high-quality images were not obtained at the optimum semiangle because of factors such as higher-order lens aberrations (Kotaka, 2009). In addition, with regard to the angular range for the ADF detector, the effect of the elastic scattering influences the image up to higher angles as the convergent semiangle increases. A decrease in the elastic scattering is indispensable for an HAADF STEM image, thus we made the inner detector angle large. The illumination system of the microscope was precisely aligned so as to obtain coma- and astigmatism-free conditions (Kuramochi, Yamazaki *et al.*, 2008). The effect of the C_c coefficient cannot be ignored in the C_s-corrected HAADF STEM images. In this study, the C_c coefficient was measured to be 1.74 mm from a

one-frame through-focal HAADF STEM image (Kuramochi *et al.*, 2009). Image processing was performed by the maximum entropy method (MEM) and the averaging method (Kuramochi, Suzuki *et al.*, 2008).

The simulations of HAADF STEM images were carried out using the method developed by Watanabe *et al.* (Watanabe, Yamazaki, Hashimoto & Shiojiri, 2001; Yamazaki, Watanabe *et al.*, 2006). This method rapidly simulates HAADF STEM images formed by both coherent Bragg scattering and incoherent TDS, simultaneously or separately. In the present simulations only the contribution from TDS was calculated, as that from Bragg scattering is negligible because of the high inner detector angle. Our dynamical simulations were performed with 283 zeroth-order and no higher-order Laue-zone reflections for the simulation of the fundamental unit cell of the Co_3O_4 spinel structure. The incident convergent beams with a small (convergent semiangle 11.2 mrad) and large semiangle (convergent semiangle 20 mrad) comprised 363 and 1151 partial incident waves, respectively. These values are large enough to describe the exact wavefields and incident probe functions onto the specimen used for STEM imaging. Furthermore, the values of the mean-square thermal vibration of the Co and O atoms are set to 0.0052 $Å^2$ (Roth, 1964). The influence of the difference in mean-square thermal vibration of O on the intensity relationship of the atomic columns constructed by Co atoms is thought to be small because the atomic number of O is very small compared with that of Co.

3. Results and discussion

Experimental convergent-beam electron-diffraction (CBED) patterns of [011]-oriented Co_3O_4 obtained from three different thickness points are shown in Figs. 1(*a*)–(*c*). The thickness at each observed point was estimated by comparing the experimental and simulated CBED patterns, where the intensities and/or patterns of each CBED disc are used as the criterion for comparison (Mader & Rečnik, 1998; Yamazaki *et al.*, 2008). The corresponding best-matching simulated CBED patterns are shown in Figs. 1(*d*)–(*f*). The thicknesses at these points were determined to be 8, 32 and 70 nm, respectively. The measurement accuracy is roughly estimated by the interval of thickness of simulated CBED patterns for the pattern fitting. In the present study, the interval of thickness is 5 nm, which is the same value as in our previous work (Yamazaki *et al.*, 2008). Figs. 1(*g*)–(*i*) show experimental raw HAADF STEM images of [011]-oriented Co_3O_4 corresponding to the points shown in Figs. 1(*a*)–(*c*). In the present observation, although the sample is polycrystalline, tiny domains which can be considered as single-crystal regions were observed. Therefore, because the observed positions are confirmed from the domain shapes and boundary positions, the respective CBED patterns and HAADF STEM images were taken from almost the same region. The processed images of Figs. 1(*g*)–(*i*) are displayed in Figs. 1(*j*)–(*l*), respectively. These images were obtained under the near Scherzer focus condition. The Co columns projected along the [011]

direction are classified into three types. The first site, called site A, has two Co atoms in the projected atomic column per unit cell. The second and third sites, called site B and site C, respectively, have one Co atom in the projected atomic column per unit cell. The difference between the sites B and C is caused by the symmetry of the atomic arrangement. Sites A, B and C are denoted by circles, squares and triangles, respectively, in Fig. 1(j). As mentioned above, the image intensities of an HAADF STEM image are considered to be dependent on the average atomic number in the projected atomic columns under a suitable lens condition. The atomic columns of sites A, B and C only contain Co atoms, and the number of atoms at site A is twice that at sites B and C. Therefore, the intensity at site A is expected to be greater than that at sites B and C. In the experiment, the intensity at site A was found to be greater than that at sites B and C, as shown in Fig. 1(j); however, the intensities at sites B and C were greater than that at site A in Figs. 1(k) and (l). As an example of a situation in which a HAADF STEM image does not correspond to the projected atomic structure, an artificial bright spot taken under an unsuitable defocus value has already been reported (Watanabe, Yamazaki, Kikuchi *et al.*, 2001). However, intensity reversal with respect to the thickness has been observed in an HAADF STEM image despite a suitable lens condition. Figs. 1(m)–(o) show simulated HAADF STEM images corresponding to the HAADF STEM images of Figs. 1(j)–(l). These simulated results are calculated for $C_s = 1.1$ mm, $\Delta f = -50$ nm and $\alpha = 11.2$ mrad. The simulations also
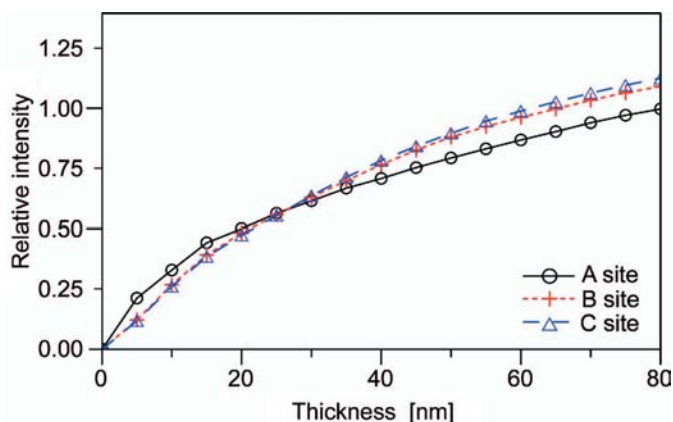
Figure 2
The simulated intensities at sites A, B and C of a C_s-uncorrected HAADF STEM image of [011]-oriented Co_3O_4 as a function of the sample thickness. Intensities are relative to the intensity on site A at 80 nm thickness.

suggest that the intensity reversal is caused by the sample thickness. In order to investigate the intensity reversal in detail, the image intensities at each site are plotted as a function of the thickness in Fig. 2. The intensity at site A is greater than that at sites B and C up to almost 30 nm, following which it becomes lower. Although the quantitative agreement is not good due to the poor crystallinity of the present sample, the simulated images qualitatively reproduce the characteristics of the experimental results.
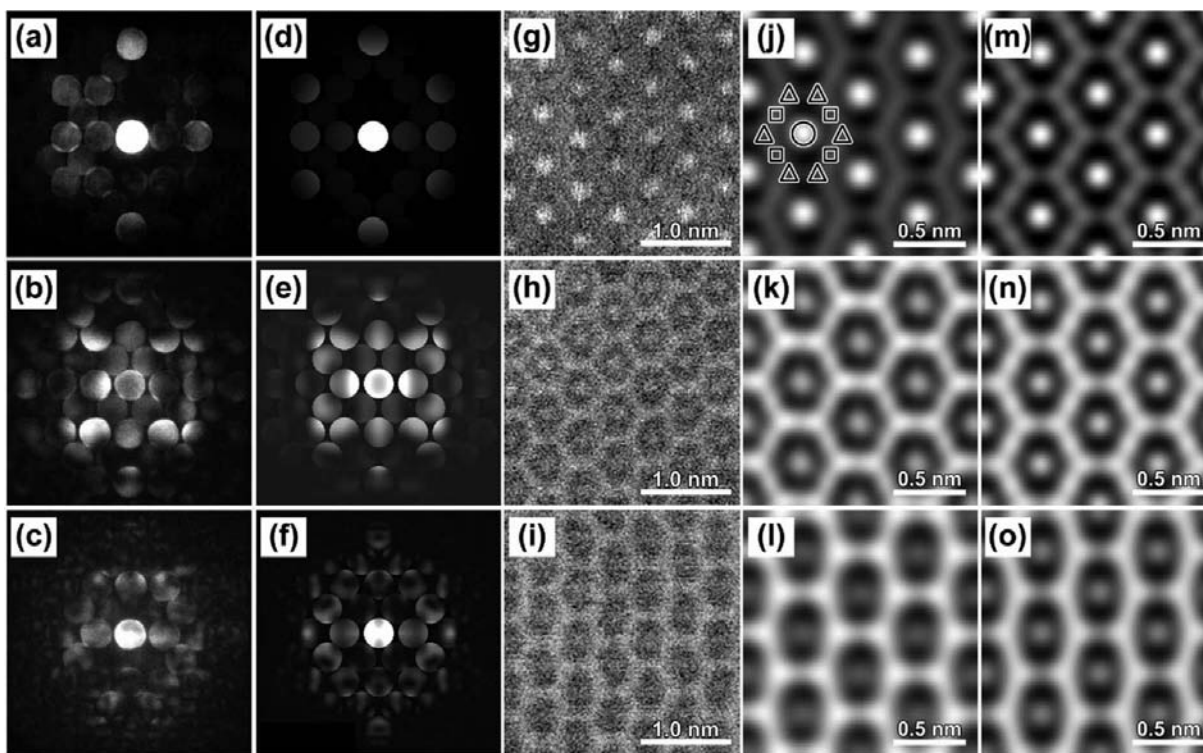
Figure 1
(a–c) Experimental CBED patterns of [011]-oriented Co_3O_4 at thicknesses of 8, 32 and 70 nm, respectively, and (d–f) simulated CBED patterns of [011]-oriented Co_3O_4 at the same thicknesses. (g–i) Experimental raw HAADF STEM images at the observed points shown in (a–c). (j–l) are the corresponding processed and enlarged HAADF STEM images, and (m–o) are the corresponding simulated HAADF STEM images.

In order to discuss this result only from the theoretical approach, two-dimensional Bloch wavefields into the sample are calculated for plane-wave illumination along a direction perpendicular to the entrance surface. The wavefield at the entrance surface is

$$\Phi(\mathbf{R}) = \sum_j \sum_g \alpha^j C_g^j \exp(i\mathbf{g} \cdot \mathbf{R}), \qquad (1)$$

where $\mathbf{R}$ is the two-dimensional position vector onto the surface, α^j are the excitation amplitudes of the jth Bloch state and C_g^j are the Bloch-wave coefficients of the jth Bloch state for Bragg reflection $\mathbf{g}$. The real parts of the wavefields for the first to ninth Bloch states are shown along with the projected crystal potential map and the dispersion surface in Fig. 3. For perpendicular incidence, the first Bloch state clearly locates on site A, and the second to fifth Bloch states locate on sites B and C. In this manner, Bloch-wave states with a larger value of k_z locate on the characteristic atomic sites. Because the purpose of this study is to investigate the intensity relationship

between site A and site B (or C) occupied only by Co atoms, the Bloch wavefields are divided into two groups in order to simplify the interpretation for the convergent case: one is constructed by the first Bloch state and the other by the second to fifth Bloch states.

In an HAADF STEM image, the wavefield due to the incident convergent beam must be considered. The general convergent wavefield on the entrance surface is

$$\Psi(\mathbf{R}, \mathbf{R}_0) = \int A(\mathbf{K}) \sum_j \sum_g \alpha^j(\mathbf{K}) C_g^j(\mathbf{K})$$
$$\times \exp\{i[\mathbf{K} \cdot (\mathbf{R} - \mathbf{R}_0) + \mathbf{g} \cdot \mathbf{R}]\}\exp[-iW(\mathbf{K})]\, d\mathbf{K}, \qquad (2)$$
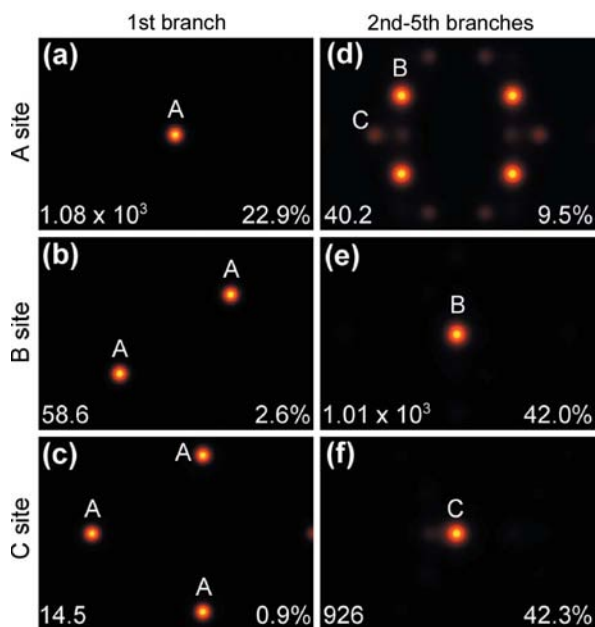
where $\mathbf{K}$ is the surface-parallel component of the partial incident wave, $A(\mathbf{K})$ is the aperture function, $\mathbf{R}_0$ is the position vector of the incident-beam position and $W(\mathbf{K})$ is the lens aberration function. In order to compare the excited Bloch states for C_s-uncorrected HAADF STEM, the intensities of
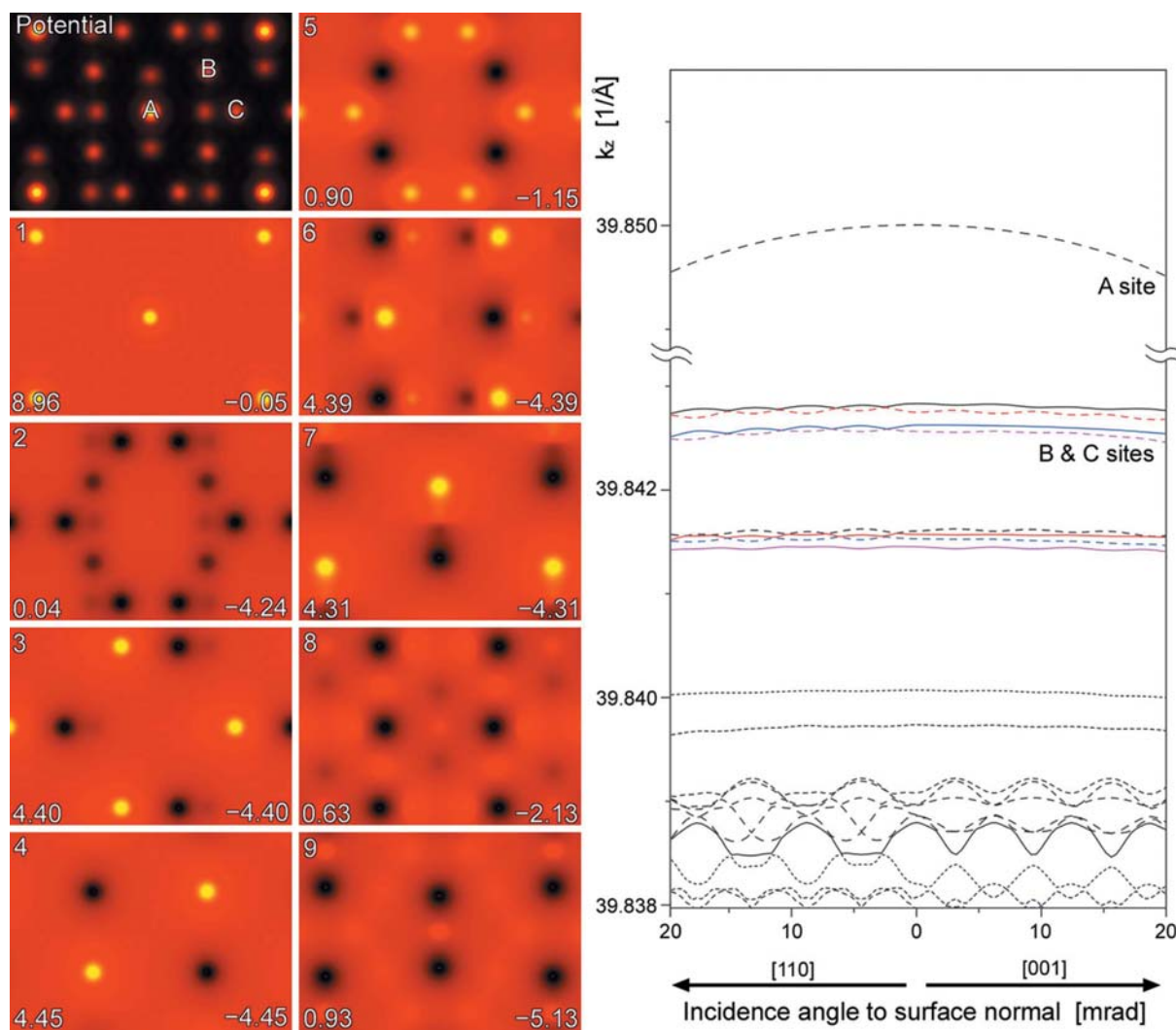
Figure 3
Left: The top left image is a map of the projected crystal potential. Thickness-independent real parts for the first to ninth Bloch states are then shown. The numbers at the top left of each indicate the Bloch-state index j, and the maximum and minimum values in each Bloch state are given at the bottom left and bottom right of each image, respectively. Right: The dispersion surface of the first and second Bloch states along the [001] and [110] directions.
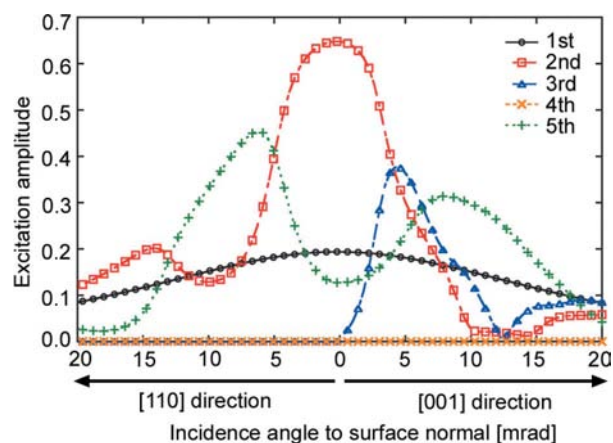
convergent Bloch wavefields for the first and the second to fifth Bloch states at each atomic site are shown in Fig. 4. These simulated results are calculated for $C_s = 1.1$ mm, $\Delta f = -50$ nm and $\alpha = 11.2$ mrad. Figs. 4(a)–(c) show the intensities constructed by the first Bloch state when the convergent incident beam illuminates sites A, B and C, respectively. Figs. (d)–(f) show the intensities constructed by the second to fifth Bloch states when the convergent incident beam illuminates sites A, B and C, respectively. Although there are some contributions from the other Bloch states, these are ignored in the qualitative interpretation. The numbers shown at the bottom left of each figure indicate the maximum intensities, and those shown at the bottom right indicate the integrated intensities over the displayed area. These integrated intensities are expressed as a percentage of the illuminating electron probe intensity on the surface. The maximum intensities at each site hardly change and the percentage of integrated intensity for the second to fifth Bloch states (Figs. 4e and f) is twice that of the first Bloch state (Fig. 4a). Furthermore, it should be noted that these percentages are less than 50%. This implies that the incident convergent electrons easily transfer to the atomic columns. In particular, when the incident convergent beam is located on site A, this phenomenon is evident. If incident convergent electrons are almost trapped at the atomic column of the incident position of the convergent beam, the HAADF STEM intensities and maximum intensities of the convergent wavefields may be strongly dependent on the average atomic number in the atomic column.

However, under the present experimental conditions, the electrons did not behave in this manner. This behavior of channeling electrons may cause the intensity reversal with the sample thickness.

In order to clarify why the present convergent beam constructs localized electrons not depending on the atomic number, the excitation amplitudes of the respective Bloch states are plotted in Fig. 5 as a function of the incident beam direction. For ease of viewing, the magnitude of the surface-parallel component of the incident beam is substituted by the

Figure 5
Excitation amplitudes for the respective Bloch states. This plot is calculated along the [110] and [001] directions.
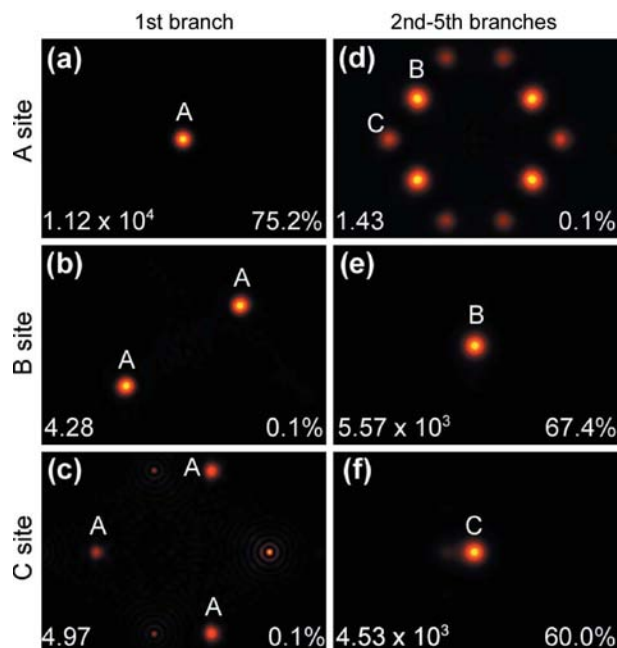

Figure 4
(a–c) The intensities of convergent wavefields constructed by only the first Bloch state when the incident beam is located on sites A, B and C, and (d–f) the intensities of the convergent wavefields constructed by the second to fifth Bloch states when the incident beam is located on sites A, B and C. The incident convergent beam is focused by the C_s-uncorrected magnetic lens.

Figure 6
(a–c) The intensities of the convergent wavefields constructed by only the first Bloch state when the incident beam is located on sites A, B and C, and (d–f) the intensities of the convergent wavefields constructed by the second to fifth Bloch states when the incident beam is located on sites A, B and C. The incident convergent beam is focused by the C_s-corrected magnetic lens.

semiangle of the incident convergent beam. For small semiangles ($\alpha = 11.2$ mrad), it should be noted that the intensity of the excitation amplitude of the first Bloch state is smaller than those of the second to fifth Bloch states. This fact is reflected in the percentages of integrated intensities, as shown in Figs. 4(a) and (b); sites B and C easily trap electrons due to their large excitation amplitudes. In addition, since the percentages of integrated intensities at sites A, B and C are less than 50%, as mentioned above, the well known cross-talk phenomenon, where Bloch states irrelevant to the incident probe position are excited, occurs. Therefore, it is necessary to set the semiangle to more than 20 mrad for trapping electrons on each atomic column around the incident probe position. In other words, an incident convergent beam having an insufficient semiangle does not result in localized intensities depending on the average atomic number in the projected atomic columns if the behavior of each excitation amplitude with the semiangle is different. Of course, this contrast-intensity reversal is expected in other crystals.

Fortunately, a large semiangle can be achieved using a recently developed C_s corrector. The intensities of the convergent wavefields at three atomic sites calculated by $C_s = -0.5$ µm, $\Delta f = 0$ nm and $\alpha = 20$ mrad are shown in Fig. 6 in a manner similar to that in Fig. 4. The integrated intensity (shown at the bottom right of each figure) and maximum intensity (shown at the bottom left of each figure) of the convergent wavefield at site A (Fig. 6a) are higher than those at sites B and C (Figs. 6e and f, respectively). This behavior with a larger convergent semiangle is greatly different from the result shown in Fig. 4. For $C_s = -0.5$ µm, a simulation with $\alpha = 11.2$ mrad produces results similar to those shown in Fig. 4; therefore, it is concluded that the difference is caused mainly by the effective semiangle of the incident convergent beam.
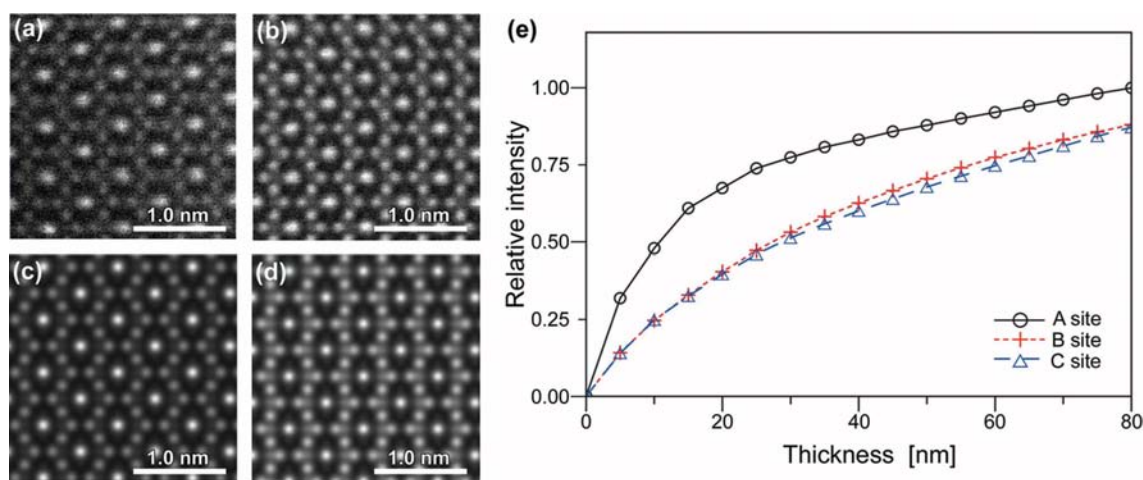
Figs. 7(a) and (b) show experimental C_s-corrected HAADF STEM images of [011]-oriented Co_3O_4 in the thin and thick region, respectively. The sample thicknesses were roughly estimated from the zero-loss spectrum by electron-energy-loss spectroscopy to be approximately 20 nm and more than 60 nm. Although a conventional HAADF STEM image indicates intensity reversal at a thickness of 60 nm, intensity reversal does not occur when a large semiangle is used. The corresponding simulated HAADF STEM images are shown in Figs. 7(c) and (d). These simulated results are calculated for $C_s = -0.5$ µm, $\Delta f = 0$ nm and $\alpha = 20.0$ mrad. The simulations also indicate that the intensity reversal is not caused by the sample thickness, and the bright-spot intensity depends on the average atomic number. In Fig. 7(e), the intensity relationship between sites A, B and C is shown in the same manner as in Fig. 2. It is confirmed that an intuitive atomic resolved image is obtained at a thickness of more than 80 nm using a large semiangle.

4. Summary

Intensity reversal with sample thickness is experimentally demonstrated in the C_s-uncorrected HAADF STEM image of [011]-oriented Co_3O_4. Improving the optimum semiangle using a C_s corrector leads to bright-spot intensities that depend on the average number of atoms in the projected atomic column. This fact is confirmed by a theoretical analysis based on the Bloch-wave description. When the behavior for each Bloch state constituting the localized intensity of each atomic column differs significantly with the semiangle of the convergent incident beam, an insufficient semiangle mainly determined by the C_s value cannot always reproduce localized intensities depending on the average atomic number of the atoms in the projected atomic column. This fact implies that the compositional analysis of defects requires a detailed comparison with dynamical simulations.

Figure 7
(a, b) Experimental C_s-corrected HAADF STEM images of [011]-oriented Co_3O_4 in the thin and thick regions, and (c, d) their corresponding simulated HAADF STEM images. (e) The simulated intensities at sites A, B and C as a function of the sample thickness. Intensities are relative to the intensity on site A at 80 nm thickness.

References

Anderson, S. C., Birkeland, C. R., Antist, G. R. & Cockayne, D. J. H. (1997). *Ultramicroscopy*, **69**, 83–103.

Batson, P. E., Dellby, N. & Krivanek, O. L. (2002). *Nature (London)*, **418**, 617–620.

Dellby, N., Krivanek, L., Nellist, D., Batson, E. & Lupini, R. (2001). *J. Electron Microsc.* **50**, 177–185.

Falke, U., Bleloch, A., Falke, M. & Teichert, S. (2004). *Phys. Rev. Lett.* **92**, 116103.

Haider, M., Uhlemann, S., Schwan, E., Kabius, B. & Urban, K. (1998). *Nature (London)*, **392**, 768–769.

Howie, A. (1979). *J. Microsc.* **117**, 11–23.

Hutchison, J. L., Titchmarsh, J. M., Cockayne, D. J. H., Mobus, G., Hetherington, C. J., Doole, R. C., Hosokawa, F., Hartel, P. & Haider, M. (2002). *Microsc. Microanal.* **8**, 10–11.

Ishizuka, K. (2001). *Ultramicroscopy*, **90**, 71–83.

Kawasaki, M., Yamazaki, T., Sato, S., Watanabe, K. & Shiojiri, M. (2001). *Philos. Mag. A*, **81**, 245–260.

Kirkland, E. J., Loane, R. F. & Silcox, J. (1987). *Ultramicroscopy*, **23**, 77–96.

Kotaka, Y. (2009). *Ultramicroscopy*. Submitted.

Kuramochi, K., Suzuki, K., Yamazaki, T., Mitsuishi, K., Furuya, K., Hashimoto, I. & Watanabe, K. (2008). *Ultramicroscopy*, **109**, 96–103.

Kuramochi, K., Yamazaki, T., Kotaka, Y., Kikuchi, Y., Hashimoto, I. & Watanabe, K. (2008). *Ultramicroscopy*, **108**, 339–345.

Kuramochi, K., Yamazaki, T., Kotaka, Y., Ohtsuka, M., Hashimoto, I. & Watanabe, K. (2009). *Ultramicroscopy*, **110**, 36–42.

LeBeau, J. M., Findlay, S. D., Allen, L. J. & Stemmer, S. (2008). *Phys. Rev. Lett.* **100**, 206101.

LeBeau, J. M., Findlay, S. D., Wang, X., Jacobson, A. J., Allen, L. J. & Stemmer, S. (2009). *Phys. Rev. B*, **79**, 214110.

Li, Z. Y., Young, N. P., Di Vece, M., Palomba, S., Palmer, R. E., Bleloch, A. L., Curley, B. C., Johnston, R. L., Jiang, J. & Yuan, J. (2007). *Nature (London)*, **451**, 46–49.

McGibbon, M. M., Browning, N. D., Chisholm, M. F., McGibbon, A. J., Pennycook, S. J. & Dravid, V. P. (1994). *Science*, **266**, 102–104.

Mader, W. & Rečnik, A. (1998). *Phys. Status Solidi A*, **166**, 381–395.

Mitsuishi, K., Kawasaki, M., Takeguchi, M. & Furuya, K. (1999). *Phys. Rev. Lett.* **82**, 3082–3084.

Nakanishi, N., Kikuchi, Y., Yamazaki, T., Okunishi, E., Watanabe, K. & Hashimoto, I. (2004). *Phys. Rev. B*, **70**, 165324.

Ohtomo, A., Muller, D. A., Grazul, J. L. & Hwang, H. Y. (2002). *Nature (London)*, **419**, 378–380.

Peng, L.-M., Dudarev, S. L. & Whelan, M. J. (2004). *High-Energy Electron Diffraction and Microscopy*. Oxford University Press.

Pennycook, S. J. & Boatner, L. A. (1988). *Nature (London)*, **336**, 565–567.

Pennycook, S. J. & Jesson, D. E. (1990). *Phys. Rev. Lett.* **64**, 938–941.

Pennycook, S. J. & Nellist, P. D. (1999). *Impact of Electron and Scanning Probe Microscopy on Material Research*, pp. 161–207. Dordrecht: Kluwer.

Roth, W. L. (1964). *J. Phys. Chem. Solids*, **25**, 1–10.

Sato, Y., Buban, J. P., Mizoguchi, T., Shibata, N., Yodogawa, M., Yamamoto, T. & Ikuhara, Y. (2006). *Phys. Rev. Lett.* **97**, 106802.

Sawada, H., Tomita, T., Naruse, M., Honda, T., Hambridge, P., Hartel, P., Haider, M., Hetherington, C., Doole, R., Kirkland, A., Hutchison, J., Titchmarsh, J. & Cockayne, D. J. H. (2005). *J. Electron Microsc.* **54**, 119–121.

Shibata, N., Chisholm, M. F., Nakamura, A., Pennycook, S. J., Yamamoto, T. & Ikuhara, Y. (2007). *Science*, **316**, 82–85.

Smith, D. J. (2008). *Microsc. Microanal.* **14**, 2–15.

Tanaka, N., Cho, S. P., Shklyaev, A. A., Yamasaki, J., Okunishi, E. & Ichikawa, M. (2008). *Appl. Surf. Sci.* **254**, 7569–7572.

Voyles, P. M., Muller, D. A., Grazul, J. L., Citrin, P. H. & Gossmann, H.-J. L. (2002). *Nature (London)*, **416**, 826–829.

Voyles, P. M., Muller, D. A. & Kirkland, E. J. (2004). *Microsc. Microanal.* **10**, 291–300.

Watanabe, K., Yamazaki, T., Hashimoto, I. & Shiojiri, M. (2001). *Phys. Rev. B*, **64**, 115432.

Watanabe, K., Yamazaki, T., Kikuchi, Y., Kotaka, Y., Kawasaki, M., Hashimoto, I. & Shiojiri, M. (2001). *Phys. Rev. B*, **63**, 085316.

Yamazaki, T., Kashiwagi, A., Kuramochi, K., Ohtsuka, M., Hashimoto, I. & Watanabe, K. (2008). *J. Electron Microsc.* **57**, 181–187.

Yamazaki, T., Kawasaki, M., Watanabe, K., Hashimoto, I. & Shiojiri, M. (2002). *Ultramicroscopy*, **92**, 181–189.

Yamazaki, T., Kotaka, Y., Kikuchi, Y. & Watanabe, K. (2006). *Ultramicroscopy*, **106**, 153–163.

Yamazaki, T., Nakanishi, N., Rečnik, A., Kawasaki, M., Watanabe, K., Čeh, M. & Shiojiri, M. (2004). *Ultramicroscopy*, **98**, 305–316.

Yamazaki, T., Watanabe, K., Kikuchi, Y., Kawasaki, M., Hashimoto, I. & Shiojiri, M. (2000). *Phys. Rev. B*, **61**, 13833–13839.

Yamazaki, T., Watanabe, K., Kuramochi, K. & Hashimoto, I. (2006). *Acta Cryst.* A**62**, 233–236.

Yu, Z., Muller, D. A. & Silcox, J. (2004). *J. Appl. Phys.* **95**, 3362–3371.